Journal of
Materials Sciences and Applications

Research Article Open Access

Enhanced Visible Light Photocatalytic Performance of Magnetite Zno Nanoparticles Decorated with Titania and Reduced Graphene Oxide Composites Against Organic Pollutants

Hanaa Selim*

Department of Analysis and Evaluation, Egyptian Petroleum Research Institute, Nasr City, Cairo, 11727, Egypt

***Corresponding Author:** Hanaa Selim, Department of Analysis and Evaluation, Egyptian Petroleum Research Institute, Nasr City, Cairo, 11727, Egypt, Tel: 01115095326, E-mail: dr.hanaa_epri@hotmail.com

Received Date: October 06, 2023 **Accepted Date:** November 06, 2023 **Published Date:** November 09, 2023

Citation: Hanaa Selim (2023) Enhanced Visible Light Photocatalytic Performance of Magnetite Zno Nanoparticles Decorated with Titania and Reduced Graphene Oxide Composites Against Organic Pollutants. J Mater sci Appl 7: 1-17

Abstract

We have developed magnetite zinc oxide (Fe_3O_4/ZnO) nanocomposites through the solid-state method, incorporating varying doses of reduced graphene oxide (rGO) (MZR) and titanium oxide (MZT). The physical and chemical properties of these nanocomposites were investigated using XRD, FT-IR, TEM, UV-Vis, DRS, and PL spectroscopy, and their ability to degrade methylene blue (MB) in wastewater under visible light irradiation was tested. Our results demonstrated that the nanocomposite absorption is enhanced in the visible range and has a high life duration of e-/h+ at the optimum composite MZR. The photo degradation efficiency of MZR is about 95% compared to pure ZnO (12%), MZ (85%), and MZT (88%), which is 7.91 times higher than that of ZnO. Reusable studies showed that the generated MZR NC photocatalysts were stable during MB photodegradation and had useful applications for the remediation of the environment.

Keywords: Nanocomposites; Crystal Magnetite; Zno; Titanium Oxide; Reduced Graphene Oxide; Photocatalytic Activity

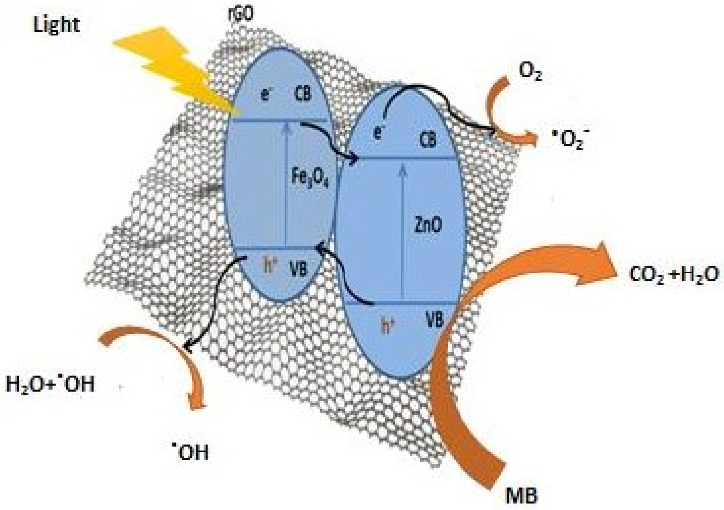

Graphical Abstract

Introduction

Wastewater generated from various industries, including paper, leather, and textile manufacturing, can contain a variety of dyes [1]. The production of these dyes poses a significant concern as the majority of them are highly detrimental to both the environment and human health [2,3]. Traditional water treatment methods, such as adsorption, chemical precipitation, and chemical oxidation, have been employed in the past, but their effectiveness has been limited. These methods have also resulted in the formation of secondary pollutants and have potential to cause significant health issues [4]. Due to the limitations of conventional water treatment methods, the photocatalytic oxidation process has gained significant importance in the field of wastewater treatment technology [2,5]. This process results in the complete decomposition of organic pollutants into water and carbon dioxide [6]. The charge carriers produced by photosynthesis in crystalline semiconductors have the potential to generate highly reactive chemical compounds such as the hydroxyl radical, which can rapidly and non-selectively degrade a wide range of organic pollutants [7,8]. Therefore, further research is necessary to optimize the photocatalytic oxidation process and improve its efficiency for practical application. Improving photocatalytic efficiency can be achieved through various approaches, such as doping different metals, e.g., Aluminium (AL) or Silver (Ag) [9-11], modifying the morphology, and combining with other metal oxides to form composites. The utilization of several semiconductors, including hexaferrites materials, MOFs [12,13], SnO_2, WO_3, TiO_2, CeO_2, and ZnO, has been widely explored for heterogeneous photocatalysis [14]. These semiconductors generally possess a wide-band-gap, necessitating the use of ultraviolet light for activation [15,16]. As a result of their promising photocatalytic properties, current research has centered on the development of exceptional semiconductor photocatalysts, such as zinc oxide (ZnO), tungsten oxide (WO_3), and titanium dioxide (TiO_2) for water splitting and degradation of organic pollutants [17,18]. ZnO is a crystalline photocatalyst that is commonly used in wastewater treatment processes due to its availability, non-toxicity, acceptable energy band regions, and excellent excitonic stability [19-22]. However, despite its advantages, ZnO also has several limitations, including a band gap that is too large, approximately 3.37 eV, which renders it incapable of visible-light photocatalytic activity, and its poor photocatalytic properties and rapid recombination of hole-electron pairs, which can result in photo-corrosion caused by the decomposition of ZnO into Zn^{2+} ions in aqueous solutions under UV irradiation [13-20]. Several research studies have attempted to enhance the properties of ZnO by addressing various limitations such as technology inadequacies, the use of carbon-based materials, doping, and the incorporation of support materials like TiO_2 and reduced graphene oxide (rGO) [23-29]. TiO_2 offers superior photocatalytic activity and has a range of applications, including waste water degradation, solar cells, and self-cleaning. TiO_2 exhibits high photoreactivity, excellent photochemical stability, non-toxicity, and environmentally friendly properties [30,31]. Reduced graphene oxide serves as an important support for ensuring a uniform distribution of ZnO without aggregation. These approaches improve ZnO photocatalytic performance by reducing the band gap absorption in the visible region, leading to excellent visible-light photocatalytic efficiency, reducing e-/h+ recombination, and suppressing ZnO photocorrosion. However, rGO/TiO_2/ZnO nanocomposites face recycling challenges. Current research is focusing on recycling nanocomposite photocatalysts with magnetic nanoparticles, such as Fe_3O_4, to overcome these difficulties and enhance performance [32-37]. In the domain of nanoparticle synthesis, the choice of magnetically-charged particles is often motivated by a desire to enhance the durability of the catalyst and prevent aggregation. A broad surface area is likewise desirable for optimal performance [37]. This investigative study presents the synthesis of crystalline magnetite ZnO photo catalysts with varying levels of graphene oxide and titania doping, employing a straightforward method. Our primary objective is to improve the photocatalytic efficiency of the synthesized material, with the ultimate aim of effectively eliminating dye pollution from water upon exposure to visible light without generating any additional pollutants. The structural, morphological, and optical properties of the resulting hybrids have been evaluated to evaluate their photocatalytic potential.

Materials and Methods

Materials

We acquired the following chemicals from Sigma-Aldrich with a purity of 99.5%: zinc zinc nitrate hexahydrate ($Zn(NO_3)_2.6H_2O$), iron chloride hexahydrate ($FeCl_3.6H_2O$), ferrous sulphate heptahydrate ($FeSO_4.7H_2O$),titanium isopropoxide (TIP), TiOCH(CH3)$_2$, graphite fine powder and potassium permanganate (KMnO4). We purchased absolute ethanol (99.8%), hydrogen peroxide (H_2O_2) (30%), sulfuric acid (H_2SO_4) (95%), sodium nitrate ($NaNO_3$) (99%), sodium hydroxide (NaOH) (98%), and methylene blue (MB) from the Honeywell company. No further purification was carried out on any of the purchased chemicals.

Under visible light irradiation, the photocatalytic activity of the MZT and MZR NCs was investigated for the degradation of MB, a model organic pollutant, in a formal experimental setup. The tests were carried out at room temperature (RT) with visible light irradiation provided by a halogen lamp (500 W). The emission spectrum of a halogen lamp ranges from 420 to 600 nm [38]. The light source was positioned 10 cm away from the cell, and a 50 mL MB solution with an initial concentration of 100 ppm was placed in a beaker. 0.1 g of each catalyst was added to the solution, and the mixture was continuously agitated in the dark for 30 min until adsorption/desorption equilibrium was achieved between the MB molecule and the catalyst molecule. The study was conducted for 90 min with continuous stirring under visible light irradiation, and the amount of MB dye degradation was measured using a UV-visible spectrophotometer (UV-1800, Shimadzu, Kyoto, Japan).

Characterization

The phase structure of the investigated samples was characterized using XRD (X-ray diffraction) with a diffractometer (Panalytical XPERT PRO MPD). CuKα radiation (λ= 1.5418 Å) was used at a rate of 40 kV and 40mA .The functional groups were detected using a Fourier transform infrared spectrometer (FT-IR) model spectrum one (Perkin Elmer, Waltham, MA, USA) with a wave number range of 400 cm^{-1}-4000 cm^{-1}. The structure and morphology of the nanocomposites were observed using JEOL JEM 2100 (JEOL, Tokyo, Japan) high-resolution transmission electron microscopy (HRTEM) at a voltage of 200 kV. A UV-Vis spectrometer (Perkin Elmer Lambda 1050, Waltham, MA, USA) was used to measure optical reflectance. The photoluminescence spectra were obtained using a Cary Eclipse fluorescence spectrophotometer (Agilent Technologies, Santa Clara, CA, USA).

Nanoparticle Synthesis

Synthesis of Crystalline ZnO Nanoparticles (Z)

The ZnO nanoparticles (ZnO NPs) were synthesized through the precipitation method [39], using an appropriate amount of Zn(NO3)2•6H2O and 25 ml of distilled water, which was stirred at 100°C for 30 min. The pH was adjusted to 12 by adding 1M NaOH and stirring for 1 h, resulting in the formation of a white precipitate. This precipitate was collected via centrifugation at 4000 rpm, and washed multiple times with deionized water and ethanol. The resulting product was then dried in an electric oven at 60°C for 6 h and air calcined at 600°C for 2 hrs.

Synthesis of Crystalline Magnetic Fe_3O_4 Nanoparticles (M)

The co-precipitation process was utilized to synthesize Fe3O4 nanoparticles. Similar to our previous study, [40] a 1:2 M ratio of ferrous and ferric salts was employed in the presence of N_2 gas. The accompanying chemical reaction is as follows:

$$2Fe^{3+} + Fe^{2+} + 8OH^{-} \rightarrow Fe_3O_4 + 4H_2O \quad (1)$$

Synthesis of Crystalline Fe_3O_4/ZnO Nanocomposites (MZ)

The co-precipitation approach was employed to synthesize Fe_3O_4/ZnO NCs. A specified ratio of iron nitrate and zinc nitrate was dissolved in 5L of deionized water (D-W). The solution was stirred vigorously while 10 ml of NaOH was added. The resulting suspension was heated to 80 °C for 2 hrs, allowed to cool at room temperature, and then magnetically separated to obtain the MZ NCs. The NCs were washed several times with a mixture of DW and ethanol and dried in an electric oven at 90 °C for 24 hours.

Synthesis of Graphene Oxide (GO)

The synthesis of GO utilized a modified version of Hummer's approach, which involved the combination of 1 g of graphite and 0.5 g of $NaNO_3$ with 23 mL of H_2SO_4 and agitation for 15 min. The graphite was then oxidized into GO through the gradual addition of 5 g of potassium permanganate ($KMnO_4$). The mixture was stirred for two hours and then heated to 98°C for 30 min. To stop the oxidation reaction and remove intermediates and remaining oxidants, the solution was treated with 60 mL of H_2O_2, resulting in a color change to brown-yellow. The resulting GO was washed three times with distilled water and dried at 60°C for 12 h [40,41].

Synthesis of Crystalline Fe_3O_4/ZnO/ rGO Nanocomposites (MZR)

A Fe_3O_4/ZnO/ rGO nanocomposite (MZR) was synthesized by a solid-state method as reported in Scheme 1. The appropriate ratio of MZ composite and rGO and then milled together, and calcined at 600°C for 4 hrs at muffle furnace [41,42].

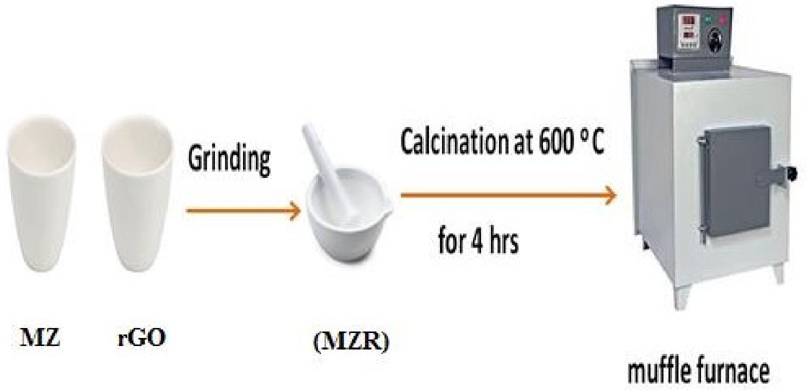

Scheme 1: Schematic Synthesis of Fe_3O_4/ZnO/ rGO nanocomposites (MZR)

Synthesis of TiO_2 Nanoparticles

The sol-gel process was employed to prepare TiO_2 nanoparticles. In a typical procedure, 600 mL of isopropanol was mixed with 100 mL of titanium isopropoxide and stirred for 20 min. Then, 1 L of distilled water was added to the solution and gently stirred for 4 hours. Finally, the gel was dried at 80°C for 48 hours and annealed in a tube furnace at 400°C for 4 hours.

Preparation of hybrid Fe_3O_4/ ZnO /TiO_2 nanocomposites (MZT)

MZT nanocomposites were fabricated by incorporating TiO_2 NPs into the MZ NCs in ethyl alcohol. The mixture was sonicated for approximately 30 minutes and dried in a vacuum oven at 65 °C for 4 hrs as shown in Scheme 2.

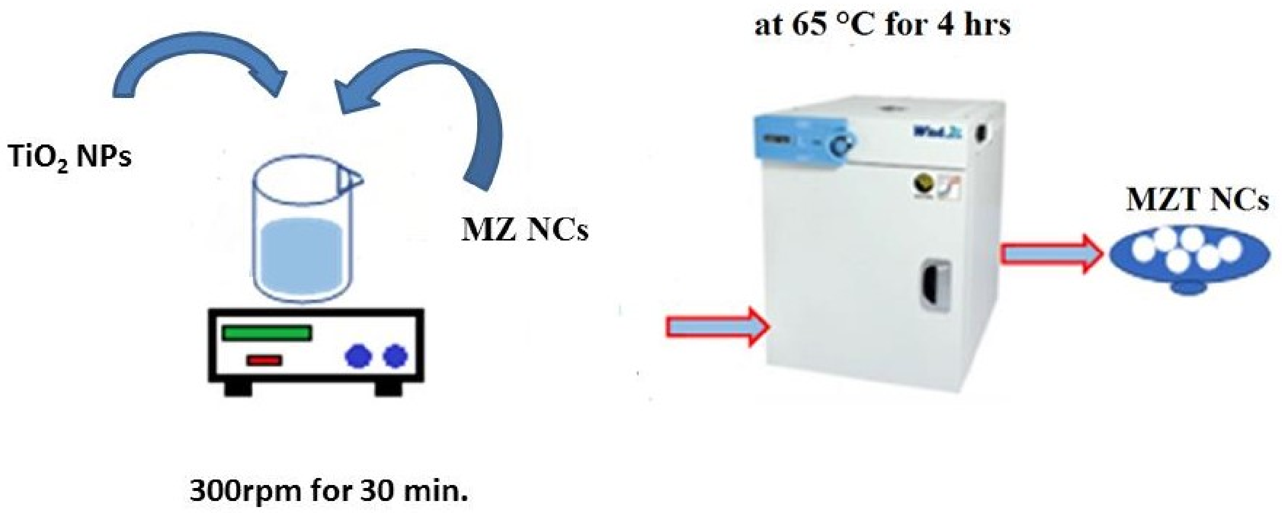

Scheme 2: Schematic Synthesis of Fe_3O_4/ ZnO /TiO_2 nanocomposites (MZT)

Results and Discussion

The crystalline phase of M, Z, MZ, MZT, and MZR was detected by X-ray diffraction (XRD), as depicted in Figure 1. The XRD pattern of ZnO exhibits the hexagonal wurtzite structure, with the planes (100), (002), (101), (102), (110), (103), (200), (112) and (201) corresponding to 2θ = 31.7, 34.4, 36.2, 47.5, 56.5, 62.8, 66.3, 67.9 and 69. 69.0°, respectively [43]. The pattern of magnetite Fe_3O_4 phase (JCPDS Card no. 01- 089-1397) with diffraction peaks at 30.00, 35.50, 43.14, 53.44, 57.40, and 62.58° corresponding to Miller indices (220), (311), (400), (422), (511), and (440), respectively [44], indicates the presence of cubic spinal structured magnetite. As shown in the curve of Fe_3O_4/ZnO (MZ), both the magnetite and zinc oxide peaks were detected. In the XRD pattern of MZR (Fe_3O_4/ZnO @RGO), the peaks of both magnetite and zinc oxide were exposed, and a small peak belonging to reduced graphene oxide was detected at $2\theta \sim 24.11°$, which was identical to the d spacing of ~0.369 nm [42]. The patterns of MZT indicate the presence of TiO_2 (anatase phase) and $ZnFe_2O_4$ (spinel phase). The diffraction pattern of anatase presented at 2θ values: 25.38, 37.82, 48.07, 53.94, 55.05, 62.74, 70.34, 75.16, and 82.33° which are matched with TiO_2 (JCPDS CARD 04-0477) crystal face of (101), (004), (200), (105), (211), (204), (220), (215), and (303), respectively. In addition, a tiny peak was observed at 35.3° which is characteristic of (311) plane of $ZnFe_2O_4$ NP.

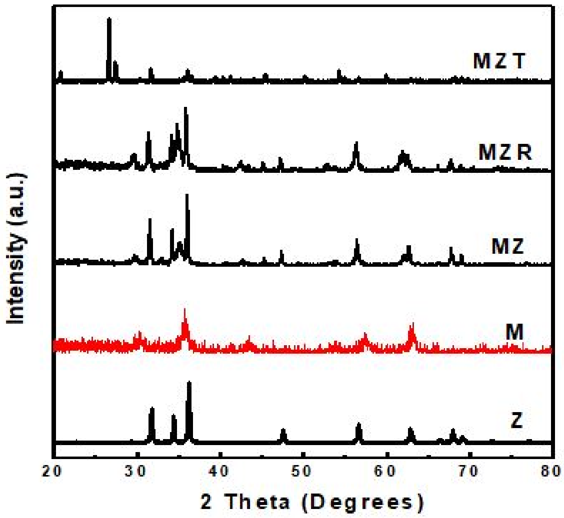

Figure 1: XRD spectra of Z, M, MZ, MZR and MZT nanocomposites

Figure 2 displays the FT-IR spectra of Z, M, MZ, MZR, and MZT NCs prior to MB degradation, which were recorded in the 400-4000 cm^{-1} region. The characteristic ZnO band is observed at 449 cm^{-1}. The weak band at 1637.8 cm-^{1} is attributed to the H-O-H bending vibration due to water absorption on the surface of nanoparticles. The stretching vibration mode of hydroxyl groups ($^{-}$OH) corresponds to the broad peak centered at 3400 cm^{-1} [45]. Additionally, the band at 568 cm^{-1} is assigned to the Fe-O bond vibration mode [46,47]. The FT-IR spectra of MZ nanocomposite are identical to those of ZnO nanocrystals hybridized with Fe_3O_4. [48] The FT-IR spectrum of the MZR NCs reveals bands at 440 and 544 cm^{-1} assigned to Zn-O and Fe-O bonds respectively, which are attributed to the creation of ZnO and Fe_3O_4 [36]. The large bands at 3440 and 1640 cm-1 are attributed to the bending and stretching modes of hydroxyl group of the H_2O. Furthermore, the band at 1460 cm-1 corresponds to M-O-G vibration [44], where M is Fe or Zn, indicating successful synthesis of Fe_3O_4, ZnO and rGO [49]. The FT-IR spectrum of MZT NCs, which reflects the existence of TiO_2, has a broad band at 420 cm^{-1}, which is attributed to the stretching mode of Ti-O-Ti, associated with octahedral coordinated titanium and $ZnFe_2O_4$. The wide band at 400 cm^{-1} is assigned to (Zn-O).

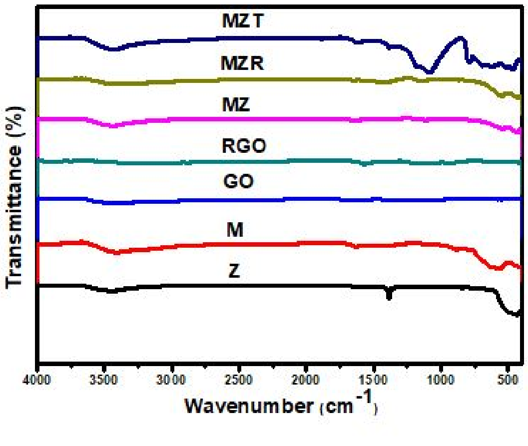

Figure 2: FT-IR spectra of Z, M, MZ, MZR, and MZT nanocomposites

In addition, a transmission electron microscope image revealed the morphology of the synthesized nanocomposites. TEM images of the Z, M, MZ, MZR, and MZT nanocomposites are presented in Figure 4 (a-e), respectively. As shown in Figure 4 (a), the ZnO nanocomposite exhibits homogeneous nanocrystalline particles with spherical shapes and slight agglomeration [50]. The TEM image of the Fe_3O_4 nanoparticles in Figure 4 (b) displays a cubic morphology [45,46]. The TEM image of the MZ composites in Figure 4 (c) shows the presence of both cubic and spherical morphologies, with average diameters of 15 nm and 20 nm for Fe_3O_4 and ZnO, respectively. The nanocomposite structure is uniform and free of accumulation. The TEM image of the MZR nanocomposite in Figure 4 (d) reveals the presence of a two-dimensional structure of RGO nanoparticles with Fe_3O_4/ZnO nanoparticles that are well-dispersed on the graphene sheet [51,52]. The TEM image of the MZT nanocomposite in Figure 4 (e) displays similar morphologies, including well-dispersed particles. The formation of multigrain agglomerations consisting of fine crystallites with irregular shapes and sizes due to their magnetic properties has been demonstrated inTiO_2 NPs as spherical shapes and Fe_3O_4/ZnO NPs as spherical shapes. Therefore, the previous analysis confirms the successful synthesis of MZR and MZT.

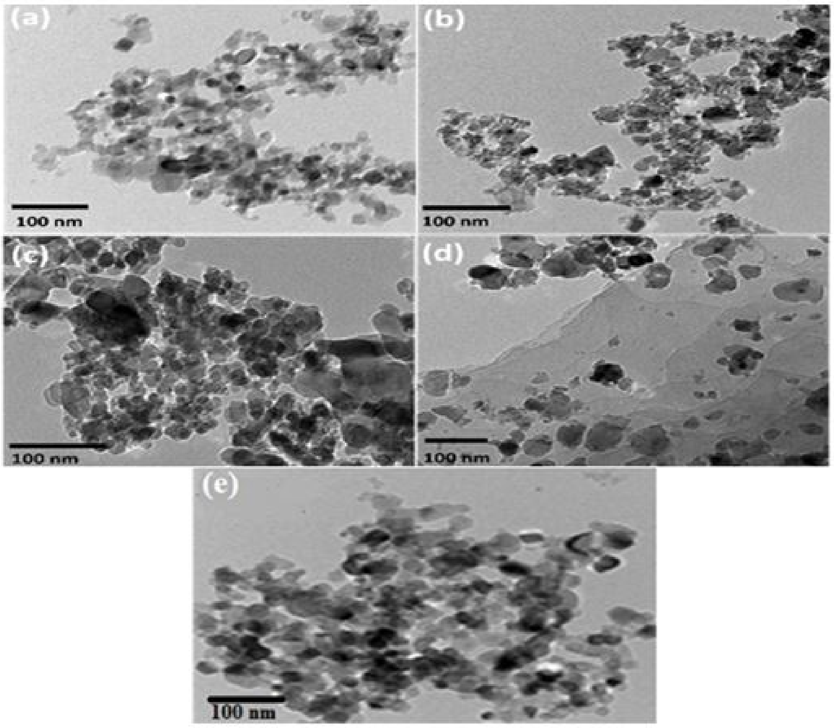

Figure 4: TEM images of Z (a), M (b), MZ (c), MZR (d) and MZT(e)

The analysis of the diffuse reflectance spectra obtained from prepared samples was conducted using UV–Vis optical spectroscopy at wavelengths ranging from 200 to 800 nm. The optical band gap of the samples was calculated utilizing the following equation:

$$\propto hv = A(hv\text{-}Eg)^{n/2} \quad (2)$$

where ʋ is the light frequency, α is the absorption coefficient, and n is the constant of proportionality. It should be noted that n = 1 for the direct transition in the prepared nanocomposite. Figure 5 displays the DRS spectra of the synthesized Z, M, MZ, MZT, and MZR NCs. The pure ZnO NP has aband gap energy of 3.20 eV. However, the presence of magnetite particles in the MZ NC resulted in a redshift of the band gap energy, as reported in Table 1. This conjugation of the two band gaps leads to increased stability for the e-/h+ pairs. The DRS spectrum of the MZT NC exhibits a slight blue shift when compared to the MZ NC, and a new, lower energy level of Eg is observed at approximately 1.9 eV. The MZR spectrum displayed a significant red shift in the presence of rGO, which was attributed to the formation of M-O-C bonds through Fe or Zn bonding with graphene, as confirmed by the FT-IR results [42]. The MZR spectrum also exhibited the lowest intensity of reflectance spectra, likely due to the higher absorption of light compared to the other samples, including Z, M, MZ, and

MZT.

Table 1: The band gap energy (Eg) values and kinetic parameters for photocatalytic activities of Z, MZ, MZT, and MZR NCs

Sample name	E_g (eV)	K_a (min^{-1})
MB	--	$4*10^{-8}$
Z	3.20	0.0014
MZ	2.07	0.0112
MZT	1.90	0.02317
MZR	1.89	0.0359

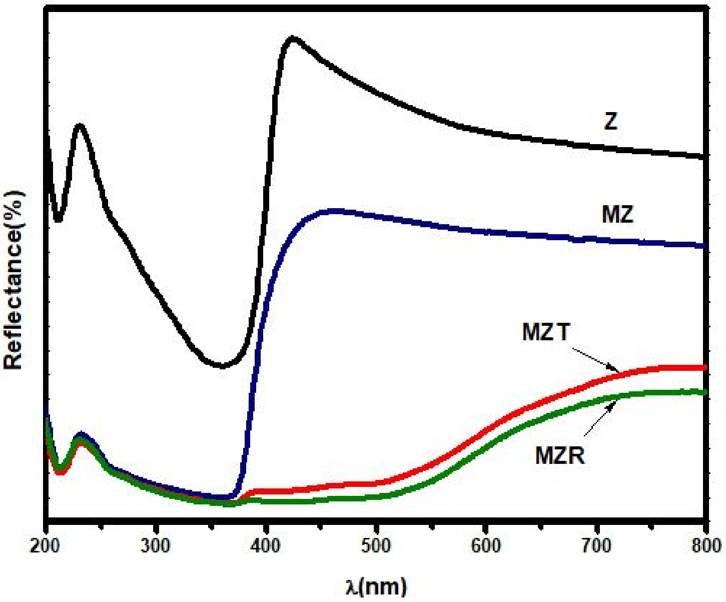

Figure 5: UV-Vis diffuse reflectance spectra of Z, MZ, MZT and MZR NCs

The analysis of the room temperature photoluminescence (PL) spectra was conducted to investigate the behavior of electron hole pairs on trapping, migration, and transfer properties. The PL spectra of Z, MZ, MZT, and MZR nanocomposites were displayed in Figure 6. The PL spectrum of pure ZnO exhibited a prominent emission band at 381 nm, along with additional peaks at 406 nm, 420 nm, and 445 nm that resulted from deep level emission (DLE) [53]. In the MZ spectrum, the PL intensity was significantly suppressed after incorporation of Fe_3O_4 with ZnO, indicating reduced recombination between photo-electrons and holes. Conversely, the emission band at 385 nm in the MZT spectrum was the result of excited electrons and holes recombination, with a decline in fluorescence intensity that clarifies the reduction in the recombination rate of holes and electrons with a high charge separation time. Moreover, the presence of Fe_3O_4 and rGO with ZnO as a triple nanocomposite exerted a synergistic effect, resulting in drastic quenching of PL intensity and an increase in the lifetime of electron stability in MZR NCs. The MZR NCs demonstrated superior photocatalytic activity compared to the other nanocomposites, suggesting that the presence of rGO enhanced the separation of charges and reduced the recombination rate of holes and electrons, leading to improved photocatalytic performance.

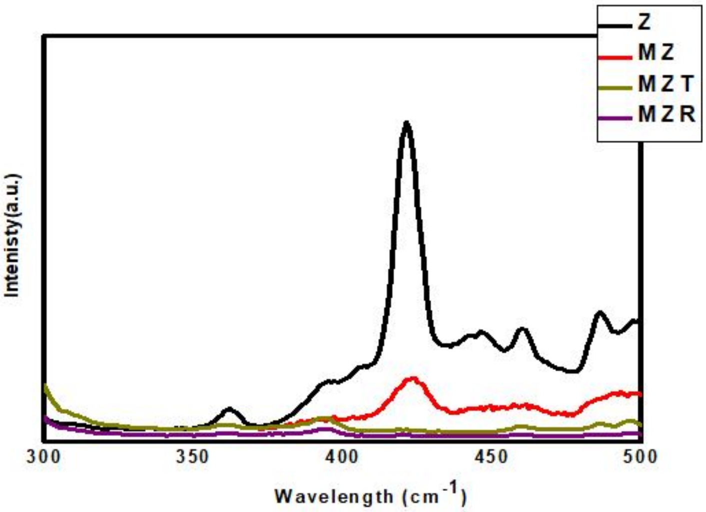

Figure 6: Photoluminescence spectra of Z, MZ, MZT and MZR NCs

The photocatalytic efficiencies of the Z, MZ, MZT, and MZR NCs were evaluated for methylene blue (MB) under visible light irradiation with a wavelength greater than 400 nm. As shown in Figure 7(a), all the prepared nanocomposites displayed significant degradation of MB concentration. MB was selected as a model organic pollutant, and the MZR NCs exhibited the highest degradation activity of approximately 95%, compared to the MZ, Z, MZT, and MZR NCs, which had photocatalytic activities of approximately 88%, 85%, and 90%, respectively. It was observed that the activity of crystalline nanocomposites depended on the amount of reduced graphene oxide (rGO) present. The higher efficiency in transportation of the photogenerated charge carriers in the MZR NCs was attributed to the aggregation of rGO layers [54,55], which was confirmed by transmission electron microscopy (TEM) and ultraviolet-visible diffuse reflectance (UV-DR) spectroscopy. These findings suggest that the incorporation of rGO into MZ NCs can significantly enhance their photocatalytic activity under visible light irradiation.

The kinetic parameters of the photodegradation of MB by the crystalline nanocomposites were analyzed using the Langmuir-Hinshelwood (L-H) first-order kinetics model. The L-H kinetics model describes the rate of reaction as a function of the concentration of the reactants, with the equation typically expressed as follows:

$$R = dC / dt = kKC / (1+KC) \quad (3)$$

Where R is the rate of reaction, dC / dt is the rate of change of the concentration of the reactants, k is the reaction rate constant, and K is the MB adsorption coefficient. The kinetic model for the degradation of MB using the prepared crystalline nanocomposites follows a pseudo--first-order pattern, with the MB concentration (C), degradation rate (r), irradiation time (t), reaction rate constant (k), and MB adsorption coefficient (K) all being important parameters. The relationship between ln(C0/C) and t, where C_0 is the initial MB concentration and C is the final MB concentration, represents the kinetics of the reaction, represents the kinetics of the reaction as following equation:

$$Ln\ (C_0/C) = k\ KT = k_a\ t$$

The values of k_a, the constant rate (min^{-1}), C_0, the initial concentration (mg L^{-1}), and C the MB concentration at time t, were obtained from the linear relation between ln (C0/C) and time as presented in Figure 7(b). The values of ka for each sample were provided in the following increasing order: MZR (0.0359 min-1) > MZT (0.02317 min-1) > MZ (0.0112 min-1) > Z (0.0014 min-1) > MB (1.4*10-8 min-1). This indicates that MZR has the highest activity. Additionally, MZR recorded the highest photocatalytic activity with illumination by visible light when compared to previous studies, as shown in Table 2.

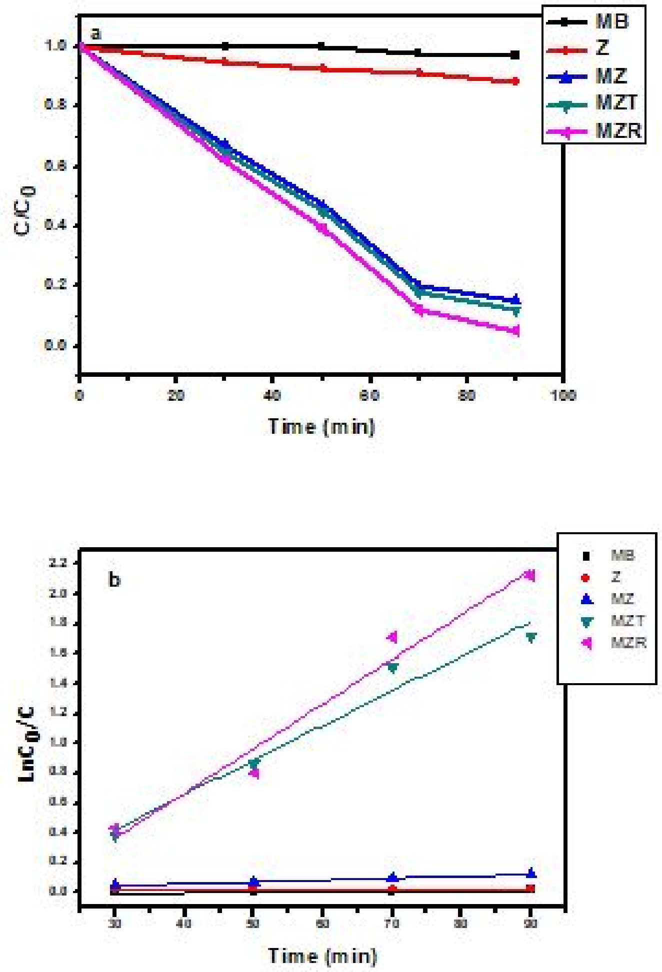

Figure 7(a): Photodegradation and (b) Kinetic of MB by Z, MZ, MZT and MZR nanocomposites for 100 ppm MB under visible light

Table 2: Photocatalytic degradation of MB under Visible Light with Various Photocatalysts

Photocatalyst	Weight of catalyst (g/L)	Concentration of MB (ppm)	Time(h)	Degradation (%)	Ref.
ZnS-TiO_2/RGO	0.4	20	2	90	[56]
WO_3/GO	0.5	3	1.2	82	[57]
Pt/WO_3/GO	0.5	3	1.2	94	[57]
Fe_3O_4 /$CdWO_4$ +H_2O_2	0.1	20	2	32	[58]
Fe_3O_4 /$CdWO_4$ /$PrVO_4$ + H_2O_2	0.1	20	2	68	[58]
Fe_3O_4/$ZnWO_4$/$CeVO_4$ +H_2O_2	0.6	25	2	84	[59]
Pt/ZnO-MWCNT	0.4	100	1	74	[60]
MZG3	2	100	1.5	95	Our work

The stability and reusability of the MZR crystalline nanocomposite in organic pollutant degradation under visible light have been consistently demonstrated through several tests, as depicted in Figure 8. The external magnet separation of the MZR crystalline nanocomposite allowed for retesting without the creation of additional pollutants. Additionally, the functional groups within the MZR crystalline nanocomposite remained stable both before and after usage, as confirmed by the Fourier Transform Infrared Spectroscopy (FTIR) results in Figure 9. As a result, the MZR crystalline nanocomposite exhibits perfect reusability with high recovery and without any secondary pollutants.

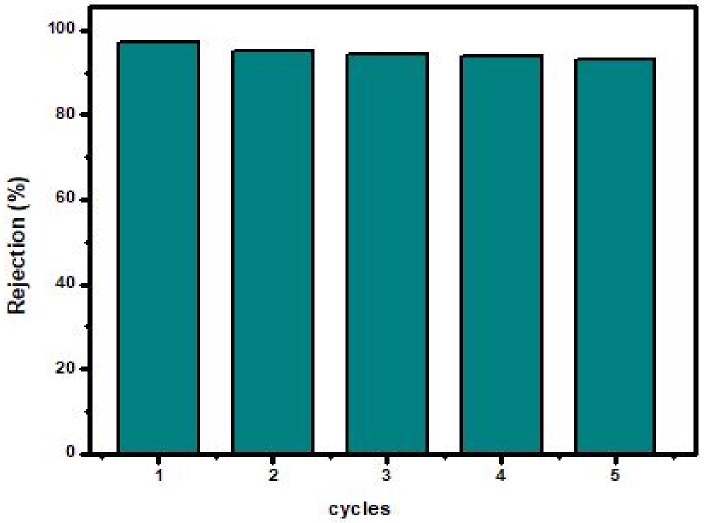

Figure 8: The MZR photocatalytic activity for degradation of organic pollutant remained stable (about 95%) throughout five consecutive cycles

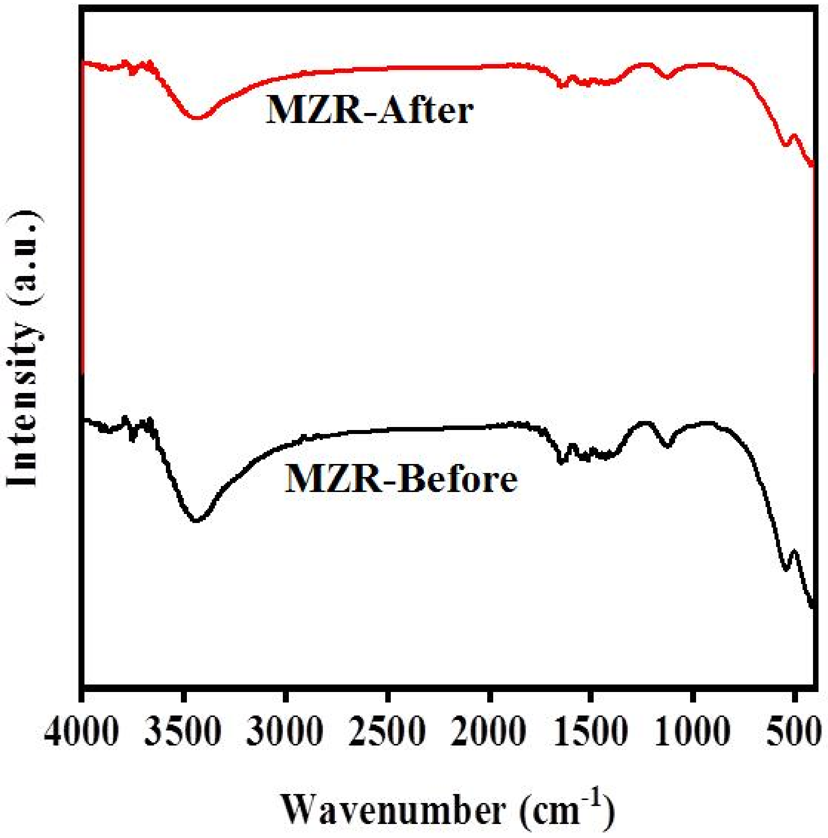

Figure 9: FT-IR spectra of MZR nanocomposites before and after of photocatalytic activity

Photocatalysis Mechanism for Degradation of Organic Pollutant by MZR Crystalline Nanocomposites

The mechanism of photocatalysis degradation based on the characterization results of MZR crystalline nanocomposites was presented in this section and is dependent on the results from previous studies. The presence of Fe_3O_4 enhances the light absorption of the catalyst, making it active in the visible region due to its small band gap energy. Furthermore, the junction between ZnO and Fe_3O_4 improves the stability of the electron/hole pairs. Additionally, the role of rGO is to capture electrons from the conduction bands of ZnO and Fe_3O_4, increasing the lifetime of the electrons and thereby enhancing the photocatalytic activity. This was recorded in the current study, and the mechanism of MZR was irradiated under visible light. The results were summarized using equations (Eq.5 to 12) and illustrated in a schematic graph (Figure 11). The MZR photo catalyst can be excited by visible light irradiation to generate electron--hole pairs (eq. 5). The electrons in the conduction band of Fe_3O_4 and ZnO are transferred to the surface of reduced graphene oxide, where rGO acts as an electron acceptor and increases the formation of oxide radicals (eq. 6) through a reduction process at the conduction band. These oxide radicals play a crucial role in the degradation of organic pollutants and the formation of hydroxyl radicals (eq. 7). The holes in the valence band of ZnO react with water molecules to form hydroxyl radicals (eqs 8-11). Finally, the organic pollutants are degraded by hydroxyl radicals to convert into environmentally friendly molecules, such as CO_2 and H_2O (eq. 12).

$MZR + h \rightarrow h^{+} + e^{-}$ (5)

$MZR + O_2 \rightarrow O_2.-$ (6)

$O_2^{\cdot-} + 2H_2O \rightarrow 4OH^{\cdot}$ (7)

$H^{+} + H_2O \rightarrow OH^{\cdot} + H^{+}$ (8)

$H_2O + H^{+}\ O_2^{\cdot-} \rightarrow H_2O_2 + OH^{\cdot}$ (9)

$H_2O_2 + e^{-} \rightarrow OH^{-} + OH^{\cdot}$ (10)

$h^{+} + OH^{-} \rightarrow OH^{\cdot}$ (11)

$OH^{\cdot}$ + organic pollutant → degradation to CO_2 + H_2O (12)

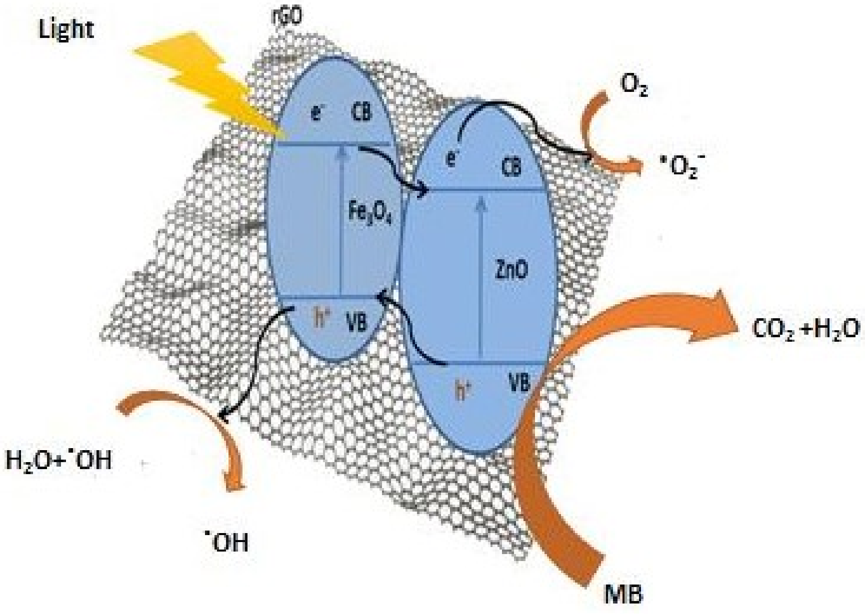

Figure 10: Schematic diagram of MB photodegradation by MZR crystalline nanocomposite under visible light

Conclusion

In this study, the Fe_3O_4/ZnO/rGO (MZR) and Fe_3O_4/ZnO/TiO_2 (MZT) nanocomposites were successfully synthesized via a solid-state process. The photocatalytic performance of MZR was investigated by degrading MB in aqueous solution under visible light irradiation. The results showed that MZR exhibited a high photocatalytic activity of approximately 95%, which was higher than that of ZnO (about 12%), MZ (about 85%), and MZT (about 88%). Additionally, MZR remained stable even after multiple uses, which was attributed to the high absorption of visible light in the presence of graphene layers and the enhancement of charge carrier stability by rGO. The XRD, FT-IR, and TEM measurements were employed to understand the structural phase of the prepared nanocomposites. The photocatalytic experimental results indicated that the reduction of the recombination efficiency of electron-hole pairs and the enhancement of visible-light-responsive photocatalytic activity of MZR nanocomposites were the main reasons for its superior photocatalytic activity, with the lowest PL intensity of MZR nanocomposite exhibiting the best photocatalytic activity. The photo degradation efficiency of MZR was about 7.91 times higher than that of pure ZnO, indicating enhanced photo-induced electron and hole separation. Moreover, MZR could be easily separated from the reaction mixture without any secondary pollutants by an external magnetic field after the photodegradation process, making it a promising photocatalyst for reducing toxic organic pollutants in wastewater.

Funding

This research received no external funding.

Data Availability Statement

All data underlying the results are available as part of the article and no additional source date are required.

Conflicts of Interest

The authors declare no conflict of interest. The funders had no role in the design of the study; in the collection, analyses, or interpretation of data; in the writing of the manuscript; or in the decision to publish the results.

References

1. Chaudhuri H, S Dash, A Sarkar (2016) Adsorption of different dyes from aqueous solution using Si-MCM-41 having very high surface area. Journal of Porous Materials 23: 1227-37.

2. Akpan UG, BH Hameed (2009) Parameters affecting the photocatalytic degradation of dyes using TiO2-based photocatalysts: a review. Journal of Hazardous Materials 170: 520-9.

3. Ravelli D et al., (2009) Photocatalysis. A multi-faceted concept for green chemistry. Chemical Society Reviews 38: 1999-2011.

4. Jou JH et al., (2014) Highly Efficient Yellow Organic Light Emitting Diode with a Novel Wet-and Dry-Process Feasible Iridium Complex Emitter. Advanced Functional Materials 24: 555-62.

5. Muruganandham M, M Swaminathan (2004) Photochemical oxidation of reactive azo dye with UV–H2O2 process. Dyes and pigments 62: 269-75.

6. Harikishore M et al., (2014) Effect of Ag doping on antibacterial and photocatalytic activity of nanocrystalline TiO2. Procedia materials science 6: 557-66.

7. Naama S et al., (2016) Enhancement of the tartrazine photodegradation by modification of silicon nanowires with metal nanoparticles. Materials Research Bulletin 76: 317-26.

8. Ayekoe CYP, D Robert, DG Lanciné (2017) Combination of coagulation-flocculation and heterogeneous photocatalysis for improving the removal of humic substances in real treated water from Agbô River (Ivory-Coast). Catalysis Today 281: 2-13.

9. Harish K, H Bhojya Naik (2013) Solar light active ZnFe2-xAlxO4 materials for optical and photocatalytic activity: an efficient photocatalyst. International Journal of Science Research 1: 301-7.

10. Wade J (2005) An investigation of TiO 2-ZnFe 2 O 4 nanocomposites for visible light photocatalysis.

11. Draz MA et al., (2021) Large scale hybrid magnetic ZnFe 2 O 4/TiO 2 nanocomposite with highly photocatalytic activity for water splitting. Journal of Nanoparticle Research 23: 1-10.

12. Elanthamilan E et al., (2023) Strontium hexaferrite microspheres: Synthesis, characterization and visible-light--driven photocatalytic activity towards the degradation of methylene blue dye 137: 113565.

13. Xia T et al., (2021) Photocatalytic degradation of organic pollutants by MOFs based materials: A review 32: 2975-84.

14. Herrmann JMJt (1999) Heterogeneous photocatalysis: fundamentals and applications to the removal of various types of aqueous pollutants 53: 115-29.

15. Lin C, KSJC Lin (2007) Photocatalytic oxidation of toxic organohalides with TiO2/UV: The effects of humic substances and organic mixtures 66: 1872-7.

16. Abo R et al., (2016) Optimized photodegradation of Bisphenol A in water using ZnO, TiO 2 and SnO 2 photocatalysts under UV radiation as a decontamination procedure 9: 27-35.

17. El-Maghrabi HH et al., (2018) Synthesis of mesoporous core-shell CdS@ TiO2 (0D and 1D) photocatalysts for solar-driven hydrogen fuel production. Journal of Photochemistry and Photobiology A: Chemistry 351: 261-70.

18. Song XC et al., (2010) Preparation and photocatalytic activity of Mo-doped WO 3 nanowires. Journal of Nanoparticle Research 12: 2813-9.

19. Ko FH et al., (2016) ZnO nanowires coated stainless steel meshes as hierarchical photocatalysts for catalytic photodegradation of four kinds of organic pollutants. Journal of Alloys and Compounds 678: 137-46.

20. Moafi HF, MA Zanjanch, AF Shojaie (2014) Lanthanum and Zirconium Co-Doped ZnO nanocomposites: synthesis, characterization and study of photocatalytic activity. Journal of Nanoscience and Nanotechnology 14: 7139-50.

21. Nishio J et al., (2006) Photocatalytic decolorization of azo-dye with zinc oxide powder in an external UV light irradiation slurry photoreactor. Journal of Hazardous Materials

138: 106-15.

22. Samah M et al., (2011) Photo-oxidation process of indole in aqueous solution with ZnO Catalyst: Study and optimization. Kinetics and Catalysis 52: 34-9.

23. Fan H et al., (2012) ZnO–graphene composite for photocatalytic degradation of methylene blue dye. Catalysis Communications 29: 29-34.

24. Elshypany R et al., (2021) Magnetic ZnO crystal nanoparticle growth on reduced graphene oxide for enhanced photocatalytic performance under visible light irradiation. Molecules 26: 2269.

25. Fattahi M et al., (2013) Vanadium pentoxide catalyst over carbon-based nanomaterials for the oxidative dehydrogenation of propane. Industrial & Engineering Chemistry Research 52: 16128-41.

26. Fattahi M et al., (2014) Kinetic modeling of oxidative dehydrogenation of propane (ODHP) over a vanadium--graphene catalyst: Application of the DOE and ANN methodologies. Journal of Industrial and Engineering Chemistry 20: 2236-47.

27. Fattahi M et al., (2015) Morphological investigations of nanostructured V 2 O 5 over graphene used for the ODHP reaction: from synthesis to physiochemical evaluations. Catalysis Science & Technology 5: 910-24.

28. Li B, H Cao (2011) ZnO@ graphene composite with enhanced performance for the removal of dye from water. Journal of Materials Chemistry, 21: 3346-9.

29. Xu T et al., (2011) Significantly enhanced photocatalytic performance of ZnO via graphene hybridization and the mechanism study. Applied Catalysis B: Environmental 101: 382-7.

30. Nasr M et al., (2017) Enhanced visible-light photocatalytic performance of electrospun rGO/TiO2 composite nanofibers. The journal of physical chemistry C 121: 261-9.

31. Schlicht S et al., (2016) An electrochemically functional layer of hydrogenase extract on an electrode of large and tunable specific surface area. Journal of Materials Chemistry A 4: 6487-94.

32. Hasanpour A et al., (2013) Dielectric behavior of Bi–Fe3O4 nanocomposite and Fe3O4 nanoparticles prepared via mechanochemical processing. Journal of magnetism and magnetic materials 346: 38-43.

33. Liu H et al., (2013) Tunable synthesis and multifunctionalities of Fe3O4–ZnO hybrid core-shell nanocrystals. Materials Research Bulletin 48: 551-8.

34. Singh S, K Barick, D Bahadur (2013) Fe 3 O 4 embedded ZnO nanocomposites for the removal of toxic metal ions, organic dyes and bacterial pathogens. Journal of Materials Chemistry A 1: 3325-33.

35. Machovsky M, I Kuritka, Z Kozakova (2012) Microwave assisted synthesis of nanostructured Fe3O4/ZnO microparticles. Materials Letters 86: 136-8.

36. Sui J et al., (2012) Synthesis and characterization of one-dimensional magnetic photocatalytic CNTs/Fe3O4–ZnO nanohybrids. Materials Chemistry and Physics 134: 229-34.

37. Liu Z, H Bai, DD Sun (2011) Facile fabrication of porous chitosan/TiO 2/Fe 3 O 4 microspheres with multifunction for water purifications. New Journal of Chemistry 35: 137-40.

38. Nada AA et al., (2017) Mesoporous ZnFe2O4@ TiO2 nanofibers prepared by electrospinning coupled to PECVD as highly performing photocatalytic materials. The journal of physical chemistry C 121: 24669-77.

39. Li YQ, SY Fu, YW Mai (2006) Preparation and characterization of transparent ZnO/epoxy nanocomposites with high-UV shielding efficiency. Polymer 47: 2127-32.

40. Nada AA et al., (2018) Elaboration of nano titania--magnetic reduced graphene oxide for degradation of tartrazine dye in aqueous solution. Solid State Sciences 78: 116-25.

41. El-Maghrabi HH et al., (2017) Magnetic graphene based nanocomposite for uranium scavenging. Journal of Hazardous Materials 322: 370-9.

42. Diab KR et al., (2018) Facile fabrication of NiTiO3/-graphene nanocomposites for photocatalytic hydrogen generation. Journal of Photochemistry and Photobiology A: Chem-

istry 365: 86-93.

43. Huo R et al., (2013) Enhanced photocatalytic performances of hierarchical ZnO/ZnAl2O4 microsphere derived from layered double hydroxide precursor spray-dried microsphere. Journal of colloid and interface science 407: 17-21.

44. Li GY et al., (2008) Kinetics of adsorption of Saccharomyces cerevisiae mandelated dehydrogenase on magnetic Fe3O4–chitosan nanoparticles. Colloids and Surfaces A: Physicochemical and Engineering Aspects 320: 11-8.

45. Shirzad-Siboni M et al., (2014) Photocatalytic reduction of hexavalent chromium over ZnO nanorods immobilized on kaolin. Industrial & Engineering Chemistry Research 53: 1079-87.

46. Sun H, L Cao, L Lu (2011) Magnetite/reduced graphene oxide nanocomposites: one step solvothermal synthesis and use as a novel platform for removal of dye pollutants. Nano Research 4: 550-62.

47. Wang L et al., (2012) Water-soluble Fe3O4 nanoparticles with high solubility for removal of heavy-metal ions from waste water. Dalton Transactions 41: 4544-51.

48. Farrokhi M et al., (2014) Application of ZnO–Fe3O4 nanocomposite on the removal of azo dye from aqueous solutions: kinetics and equilibrium studies. Water, Air, & Soil Pollution 225: 2113.

49. Benjwal P et al., (2015) Enhanced photocatalytic degradation of methylene blue and adsorption of arsenic(iii) by reduced graphene oxide (rGO)–metal oxide (TiO2/Fe3O4) based nanocomposites. RSC Advances 5: 73249-60.

50. Yu J et al., (2019) Duality in the mechanism of hexagonal ZnO/CuxO nanowires inducing sulfamethazine degradation under solar or visible light. Catalysts 9: 916.

51. Sun CL et al., (2011) The simultaneous electrochemical detection of ascorbic acid, dopamine, and uric acid using graphene/size-selected Pt nanocomposites. Biosensors and Bioelectronics 26: 3450-5.

52. El-Maghrabi HH et al., (2016) One pot environmental friendly nanocomposite synthesis of novel TiO2-nanotubes on graphene sheets as effective photocatalyst. Egyptian Journal of Petroleum 25: 575-84.

53. Oprea O et al., (2013) THE INFLUENCE OF THE THERMAL TREATMENT ON LUMINESCENCE PROPERTIES OF ZnO. Digest Journal of Nanomaterials & Biostructures (DJNB) 8.

54. Pan X et al., (2012) Comparing graphene-TiO2 nanowire and graphene-TiO2 nanoparticle composite photocatalysts. ACS applied materials & interfaces 4: 3944-50.

55. Qiu J et al., (2012) Photocatalytic synthesis of TiO2 and reduced graphene oxide nanocomposite for lithium ion battery. ACS applied materials & interfaces 4: 3636-42.

56. Qin Y et al., (2019) Photocatalytic and adsorption property of ZnS–TiO2/RGO ternary composites for methylene blue degradation. Adsorption Science & Technology 37: 764-76.

57. Ismail AA, M Faisal, A Al-Haddad (2018) Mesoporous WO3-graphene photocatalyst for photocatalytic degradation of Methylene Blue dye under visible light illumination. Journal of Environmental Sciences 66: 328-37.

58. Marsooli MA et al., (2019) Preparation and characterization of magnetic Fe3O4/CdWO4 and Fe3O4/CdWO4/PrVO4 nanoparticles and investigation of their photocatalytic and anticancer properties on PANC1 cells. Materials 12: 3274.

59. Marsooli MA et al., (2020) Synthesis of Magnetic Fe 3 O 4/ZnWO 4 and Fe 3 O 4/ZnWO 4/CeVO 4 Nanoparticles: The Photocatalytic Effects on Organic Pollutants upon Irradiation with UV-Vis Light. Catalysts 10: 494.

60. Sobahi TR et al., (2017) Photocatalytic degradation of methylene blue dye in water using Pt/ZnO-MWCNT under visible light. Nanoscience and Nanotechnology Letters 9: 144-50.